Astronomy & Astrophysics

XMM-Newton study of the star forming region NGC 1333[*]

T. Preibisch[**]

Max-Planck-Institut für Radioastronomie, Auf dem Hügel 69, 53121 Bonn, Germany

Abstract. We analyze the data of a deep *XMM-Newton* X-ray imaging observation of the NGC 1333 star forming region. The observation covered a period of about 14 hours and has a total MOS-equivalent exposure time of 235 ksec. In addition to 46 bright X-ray sources revealed by source detection routines, we find weak X-ray emission at the positions of 40 X-ray sources detected originally in a recent *Chandra* observation of NGC 1333. The *XMM-Newton* countrates of most sources agree well with their countrates in the *Chandra* data; about 80% of the sources vary by a factor of less than 3 between the two X-ray observations which are separated by 18 month. The X-ray lightcurves of several sources reveal large flares with parameters typical for X-ray active young stellar objects. We also construct and analyze the X-ray spectra of the stronger sources and derive plasma temperatures between ∼0.7 keV and ∼3 keV for the T Tauri stars in NGC 1333, and higher temperatures up to ∼12 keV for flaring sources and deeply embedded young stellar objects. We consider in detail the X-ray properties of the optically invisible infrared source SVS 16, which showed a large X-ray flare during our observation. Its X-ray spectrum confirms that the hydrogen column density towards SVS 16 is much lower than expected from the extinction determined from near-IR spectroscopy and photometry. The reason for this inconsistency remains unclear. Finally, we search for, but do not detect any X-ray emission from HH 7-11 or one of the other Herbig-Haro objects in NGC 1333. Also, none of the class 0 protostars in the region is detected in X-rays.

Key words. open clusters and associations: individual: NGC 1333 – stars: formation – stars: coronae – stars: low-mass, brown dwarfs – stars: pre-main sequence – X-rays: stars

1. Introduction

NGC 1333 is an optical reflection nebula within a highly active star forming region in the Perseus molecular cloud complex. Near infrared observations of NGC 1333 (Strom et al. 1976; Aspin et al. 1994; Lada et al. 1996) found about 150 young stellar objects that are contained within two subclusters separated by about 5′. By modeling the infrared luminosity function, Lada et al. (1996) estimated the age of the double-cluster to be no more than 10^6 years. The northern cluster contains the optically prominent reflection nebula which is mainly illuminated by the B9 star BD +30°549. The southern cluster is associated with dense molecular cloud material (e.g. Lada et al. 1974) and contains many signposts of ongoing star formation: the famous HH 7-11 outflow and numerous other Herbig-Haro objects (Herbig & Jones 1983; Bally et al. 1996; Bally & Reipurth 2001), molecular outflows and jets (Hodapp & Ladd 1995), and several extremely young class 0 protostars (Knee & Sandell 2000; Looney et al. 2000; Chini et al. 2001). The presence of numerous molecular outflows and Herbig-Haro objects suggests that a nearly coeval microburst of star formation is going on in the NGC 1333 region (Bally et al. 1996) and there is

evidence for ongoing shock driven star formation (Warin et al. 1996; Knee & Sandell 2000).

For the distance to NGC 1333 we adopt here a value of 310 pc, based on *Hipparcos* parallactic measurements of the Perseus OB2 association (318 ± 27 pc; de Zeeuw et al. 1999) and a careful determination of the distance to IC 348 (Herbig 1998), the other center of recent star formation activity in the Perseus cloud complex. The optically bright G-type star BD +30°547 in the southern part of the NGC 1333 region is probably a foreground object (Cernis 1990), perhaps related to the Taurus star forming region.

The motivation for our *XMM-Newton* study was severalfold: first, the high sensitivity of *XMM-Newton* for hard X-rays makes it well suited for a deep look through the molecular gas towards the embedded young (proto-)stars in one of the most active nearby star forming regions (for a review see Feigelson & Montmerle 1999). Second, the presence of the numerous outflows and Herbig-Haro objects in the NGC 1333 region offers an interesting opportunity to search for X-ray emission from jets and outflows. After the first X-ray discoveries of jets (Pravdo et al. 2001; Favata et al. 2002; Bally et al. 2003), the detection of similar objects would strongly improve the understanding of the processes giving rise to the observed emission. Third, we have recently performed a comparable sensitive

---

[*] Tables 1 and 2 are only available in electronic form at `http://www.edpsciences.org`

[**] e-mail: `preib@mpifr-bonn.mpg.de`
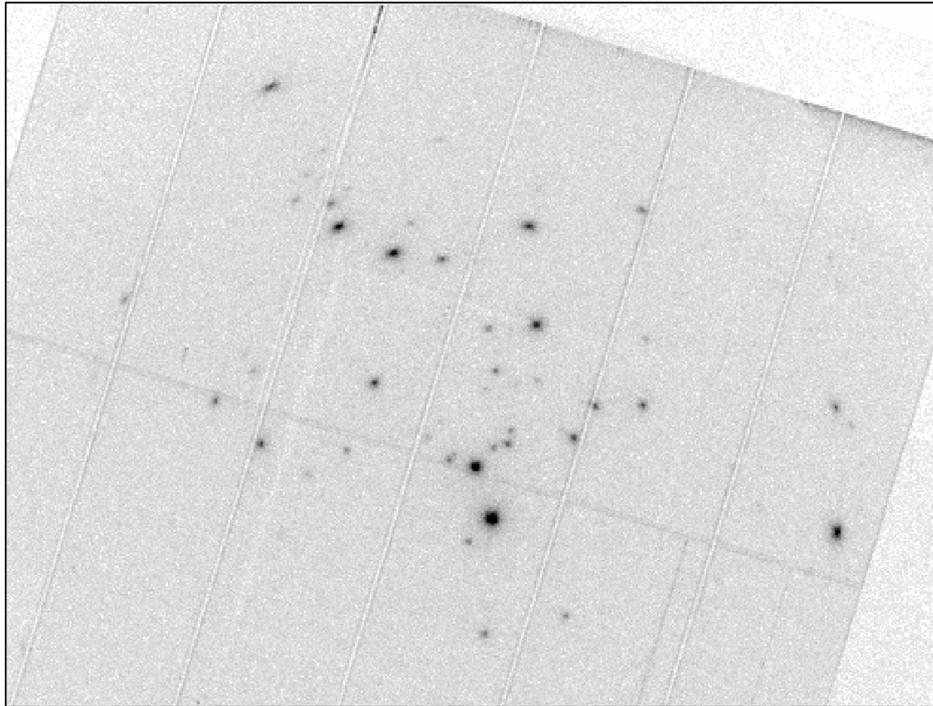
Fig. 1. The central ~26′ × 20′ region of the *XMM-Newton* image of NGC 1333. This image is the sum of the MOS1 + MOS2 + PN images, displayed with a square-root intensity scale.

X-ray study of the young cluster IC 348 (Preibisch & Zinnecker 2001, 2002), which is the other center of star formation activity in the Perseus molecular cloud complex. The comparison of these clusters allows one to study two embedded clusters in different stages of evolution.

The first X-ray observation of NGC 1333 was performed with the ROSAT HRI (Preibisch 1997). Twenty X-ray sources were detected, 16 of which are probably members of the cluster. Recently, NGC 1333 has been observed with the ACIS-I detector on board the *Chandra X-ray Observatory*. This observation, presented in Getman et al. (2002; G02 hereafter) lead to the detection of more than 100 X-ray sources down to the sensitivity limit of ~10^{28} erg/s. G02 presented identifications of the X-ray sources with optical, infrared, and submm counterparts. While 32 of these sources appear to be foreground stars and extragalactic background, 95 X-ray sources could be identified with known cluster members. G02 also performed a very comprehensive analysis of the X-ray properties of the young stellar objects in NGC 1333.

2. Observations and data analysis

NGC 1333 was observed with the European Photon Imaging Cameras (EPIC) on board *XMM-Newton*. The EPIC system (see Jansen et al. 2001) consists of two identical EPIC-MOS cameras (Turner et al. 2001) and the EPIC-PN camera (Strüder et al. 2001). The cameras were operated with the medium optical blocking filter and in the Full-Frame mode. They provide a ≈30′ diameter field-of-view, energy coverage from ≈0.15−15 keV, and moderate energy resolution ($E/\Delta E \approx$ 20−50). In comparison to *Chandra*, *XMM-Newton* offers a considerably larger effective area (2350 cm^2 at 1 keV for

EPIC compared to 700 cm^2 for *Chandra*/ACIS), especially at high energies (1400 cm^2 at 6 keV for EPIC compared to 200 cm^2 for *Chandra*/ACIS), but has a much lower spatial resolution (15″ half-energy width of the *XMM-Newton* mirror PSF compared to 0.5″ for *Chandra*).

The observation of NGC 1333 was obtained during the satellite revolution number 407 and lasted from 27 February 2002, 22:07:35 UT until 28 February 2002, 12:50:40 UT. The exposure times were 51.6 ksec for the MOS1 camera, 51.7 ksec for the MOS2 camera, and 44.8 ksec for the PN camera. As the sensitivity of the PN camera is 2.94 times higher than the individual MOS cameras for the case of the medium filter, the total MOS equivalent exposure time was 235.0 ksec. The optical monitor was turned off due to the presence of optically bright stars in the field-of-view. Extraction of science products from the Observation Data Files followed standard procedures using the *XMM-Newton* Science Analysis System (SAS). For the extraction of the counts, spectra, and lightcurves we used the SAS version 5.3.3. We first investigated the total light curves of the cameras and found several intense background flares during our observation (see Fig. 3). This flaring background is usually attributed to soft protons which are presumably funneled towards the detectors by the X-ray mirrors. We therefore created cleaned event files in which the periods of high background intensity were excluded. As this cleaning step removed nearly half of the original exposure time, the sensitivity of the cleaned data is significantly reduced. For our analysis of the count rates, lightcurves and spectra we therefore used the un-cleaned original events files; the flaring background component was corrected for by background subtraction.
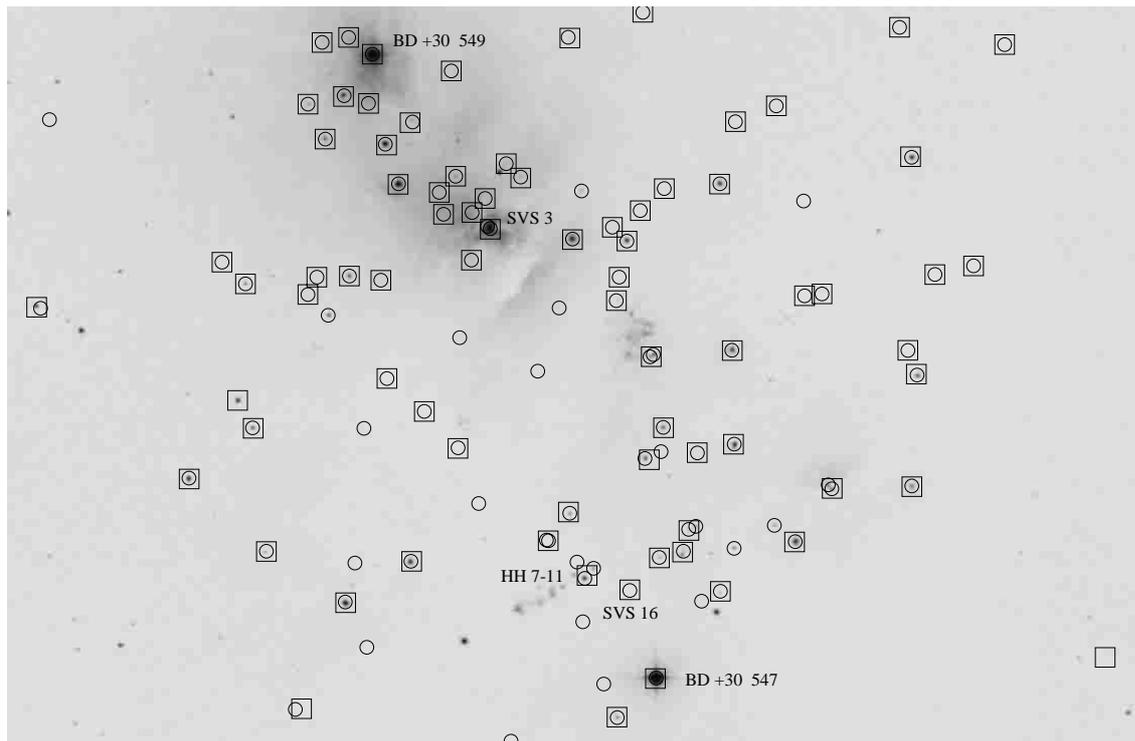
Fig. 2. Optical image of NGC 1333 (Digitized Sky Survey; field-of-view about ~20′ × 13′). The positions of the X-ray sources detected by *Chandra* (see G02) are marked by circles, the sources detected by *XMM-Newton* are marked by boxes. The objects discussed in the text are marked.

For a detailed comparison of our *XMM-Newton* data to the *Chandra* data presented by G02, we retrieved the observation files from the *Chandra* data archive and analyzed them with the CIAO 2.1.2 software package.

2.1. Source detection and identification

Our compilation of the list of X-ray source was performed in several steps. We started with a source list obtained by the standard SAS detection pipeline. This automatic detection retrieved most of the bright X-ray sources correctly, but it also "detected" many spurious sources and missed a few source that are easily visible in the image. We manually removed the obvious false detections and added the missing strong sources. Then we tried the *wavdetect* program within the CIAO data analysis system (Freeman et al. 2002) on a variety of input images (full energy band versus soft-band and hard-band images; background-flaring cleaned images versus un-cleaned images; summed MOS + PN images versus individual images). These efforts revealed several additional faint sources and finally left us with a combined list of 46 X-ray sources. We compared the source coordinates derived from the *XMM-Newton* data to optical images and found no indications for systematic errors in the X-ray source positions.

We then compared our *XMM-Newton* source list to the *Chandra* list of 109 sources given in G02 (their Table 2). Six of our 46 *XMM-Newton* sources were outside the field-of-view of the *Chandra* image. While one of the 40 *XMM-Newton* sources in the common field-of-view was not detected by *Chandra*, the

other 39 *XMM-Newton* sources can be reliably identified with *Chandra* sources. In 9 cases the much sharper *Chandra* images resolved one of our *XMM-Newton* sources into two individual X-ray sources. Taking this into account, our *XMM-Newton* source list retrieves 48 of the 109 *Chandra* sources. This means that 61 of the 109 *Chandra* sources (i.e. 56%) are "missing" in the *XMM-Newton* images. To investigate this in more detail, we determined the counts in our *XMM-Newton* images at the locations of these *Chandra* sources and compared them to the expected counts in source-free background regions. In 28 cases the sum of the counts determined in the MOS1+MOS2+PN data exceeded the background level by at least 5σ; we consider these objects as marginally detected sources. For 12 other cases the number of counts was between 3σ and 5σ above the expected background level; we consider these objects as tentative sources. For the other 21 *Chandra* sources, our *XMM-Newton* data show no indication for the existence of an X-ray source.

Table 1 provides a list of all X-ray sources in NGC 1333 detected by *Chandra* and/or *XMM-Newton*. For the *Chandra* sources we use the names of the form CXONGC1333 JHHMMSSS.s+DDMMSS defined in G02. The 7 sources only seen by *XMM-Newton* are denoted by names of the form XMMU JHHMMSSS.s+DDMMSS based on their J2000 coordinates.

2.2. Determination of countrates

With SAS we extracted the counts for all sources in 15″ radius apertures in the energy band [0.2−10] keV. This radius
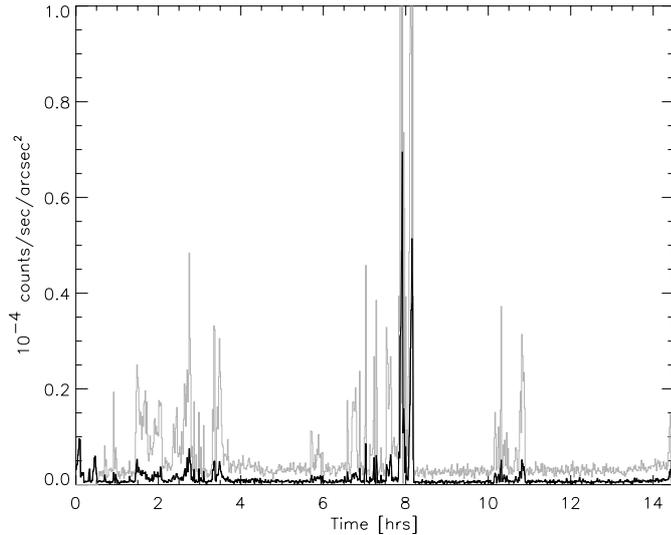
Fig. 3. Background flaring during the *XMM-Newton* observation, probably due to solar energetic particles. The black line shows the mean of the two EPIC-MOS lightcurves, the grey line shows the EPIC-PN lightcurve, extracted from two large source-free regions.

contains 70% of the point-source flux. We also determined the exposure time for each source in each detector from the corresponding exposure maps. The mean source count rates were then computed by subtracting the expected background counts, dividing by the exposure time, and applying the PSF correction factor (1/0.7). The resulting count rates are listed in Table 1. The faintest detectable sources have MOS countrates around ~0.7 cnts/ksec; the brightest source (the foreground G-type star BD +30°547) has a MOS countrate of 0.1 cnts/s and a PN countrate of 0.4 cnts/s; these numbers show that the "photon pile up" effect[1] is not a problem for our data.

At the nominal positions of the 21 *Chandra* sources that are undetected in our *XMM-Newton* data we determined the number of counts and the expected background level. We used the Bayesian statistics method described by Kraft et al. (1991) to determine 90% confidence upper limits for their count rates in our *XMM-Newton* data. For 5 of the undetected *Chandra* sources no useful upper limits could be determined because they are located at positions with very low exposure in our *XMM-Newton* images (e.g. in the gaps between individual chips or close to the edge of the image).

2.3. Comparison of Chandra and XMM-Newton countrates

The expected count rates of different detectors for a given X-ray flux can be computed with the PIMMS[2]. We computed the expected *XMM-Newton* and *Chandra*-ACIS countrates for thermal Raymond-Smith plasma-spectra with temperatures
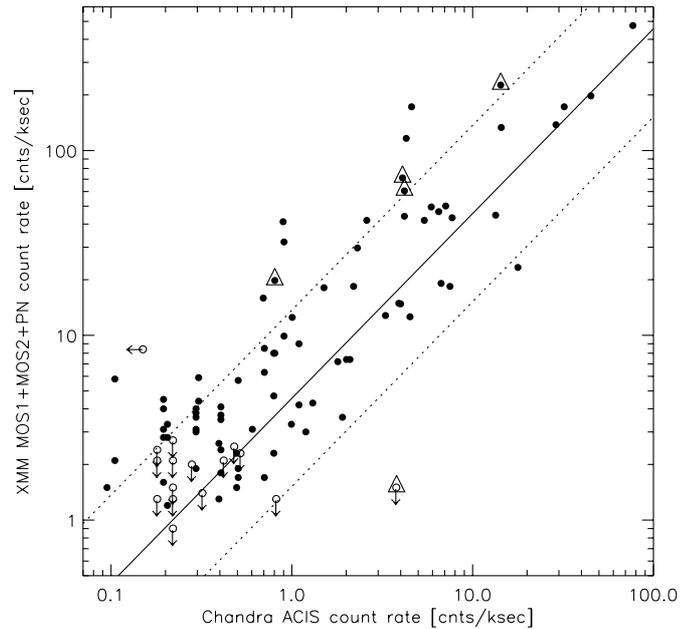
Fig. 4. Comparison of *XMM-Newton* and *Chandra* countrates for the sources in NGC 1333. Solid dots show sources detected by both observatories, open dots with arrows show upper limits for those sources that were detected by only one of the observatories. Flaring sources are marked by triangles. The solid line shows the theoretically expected relation of the countrates based on typical spectral properties of the sources (see text), the dotted lines define the band corresponding to variations by a factor of 3.

between 1 keV and 3 keV and a range of hydrogen column densities between 5×10^{21} cm^{-2} ($A_V \sim 2.5$ mag) to 5×10^{22} cm^{-2} ($A_V \sim 25$ mag). The resulting count rate ratios are not very sensitive to these parameters and vary by less than 10% around the values $CR_{MOS}/CR_{ACIS} = 1$ and $CR_{PN}/CR_{ACIS} = 2.8$.

In Fig. 4 we plot the total *XMM-Newton* count rate ($CR_{MOS1} + CR_{MOS2} + CR_{PN}$) against the *Chandra*-ACIS count rate. The solid line shows the theoretically expected relation assuming identical source luminosities at the time of the *Chandra* and *XMM-Newton* observations. As our *XMM-Newton* observation was performed more than 18 months after the *Chandra* observation, and the X-ray emission of young stars is generally variable (e.g. Montmerle et al. 1983), we expect to see some deviations from this line. The dotted lines define the band corresponding to variations by a factor of 3. The great majority of the objects lies inside this band; therefore, there is a generally good agreement between our *XMM-Newton* data and the *Chandra* data. Most of the *Chandra* sources that are undetected in our *XMM-Newton* images are among the faintest *Chandra* sources; their non-detection in our *XMM-Newton* data can probably be explained by variability. Some of those objects with large count rate differences showed a flare in either the *XMM-Newton* or the *Chandra* observation. For example, CXONGC1333 J032911.2+311718, the only object for which our *XMM-Newton* upper limit is much below the mean count rate from the *Chandra* data, showed a large flare during the *Chandra* observation (see Fig. 5 in G02, source # 67); its quiescent level is consistent with the *XMM-Newton* upper limit.
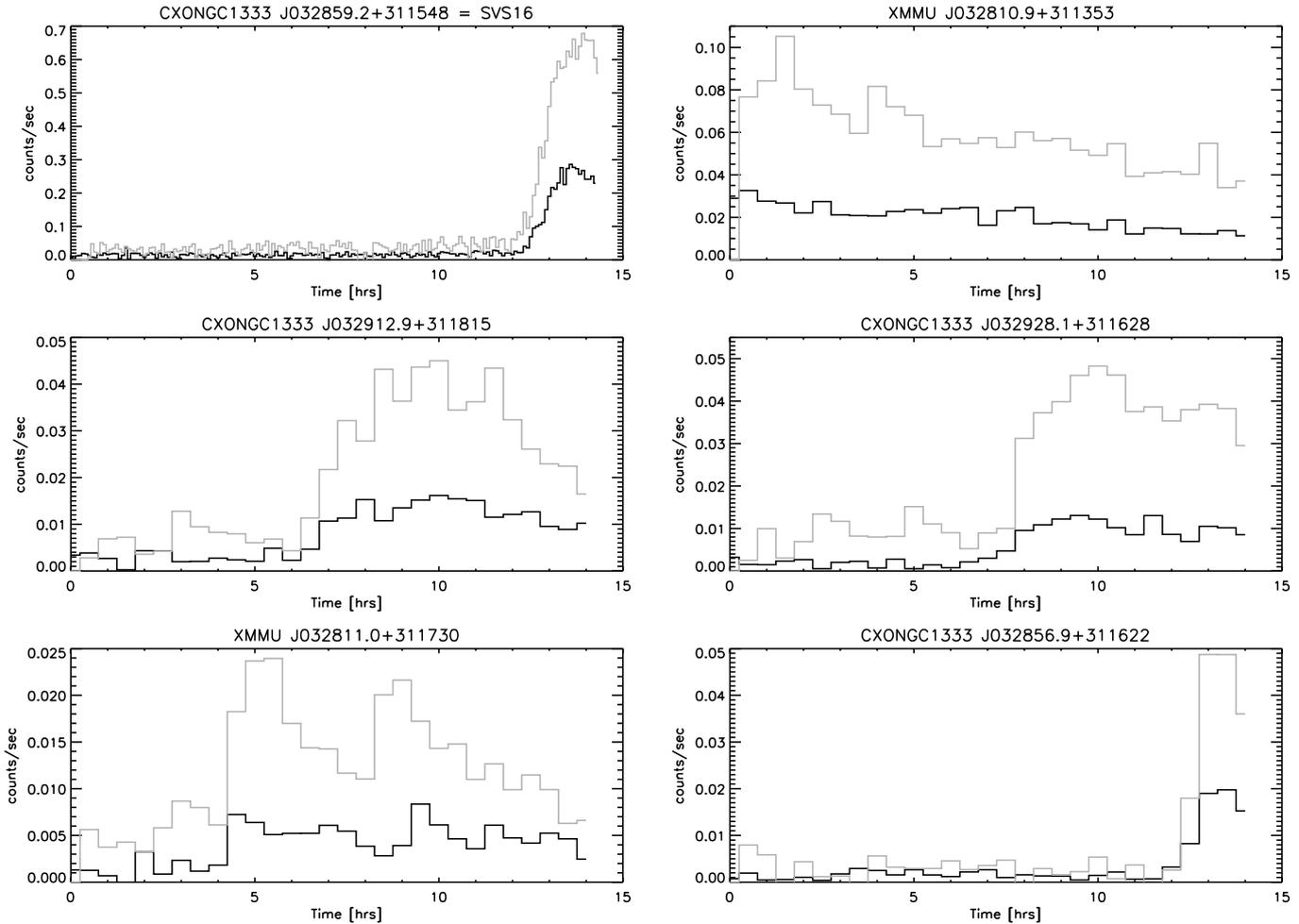
Fig. 5. Lightcurves for the sources exhibiting strong variability during our *XMM-Newton* observation. In each panel the grey histogram shows the 0.2–10 keV band background subtracted lightcurve extracted from the PN data, rebinned into 30 min bins (5 min for SVS 16). The black solid histogram shows the mean of the two MOS lightcurves.

The source XMMU J032930.4+311903, which was not seen by *Chandra* shows rather strong irregular variations during the *XMM-Newton* observation; the minimum countrate is consistent with the upper limit we determined for this source in the *Chandra* data.

2.4. Source identification

The identifications of the *Chandra* sources are listed in Table 1 of G02; for 80 out of the 109 X-ray sources optical and/or infrared counterparts could be found. For the 7 *XMM-Newton* sources not seen by *Chandra* we searched for optical and infrared counterparts. Three X-ray sources have optical counterparts, two have infrared counterparts, but for the other two we could not find any counterpart. The single *XMM-Newton* source in the common field-of-view that was not detected by *Chandra* is identified with the T Tauri star LkHα 356.

3. Temporal variability

With SAS we extracted the lightcurves for all *XMM-Newton* sources with more than ~200 counts to study their temporal

variability. In addition to the source lightcurves, we also extracted the lightcurves from two large source-free background regions. Visual inspection of the individual background-subtracted lightcurves showed irregular count rate variations in many sources. For six sources, however, we found clear evidence for systematic variability; these lightcurves are shown in Fig. 5. In most cases we see typical flares with rise and decay times of a few hours, very similar to flares on other X-ray active young stars (e.g. Montmerle et al. 1983; Preibisch & Neuhäuser 1995; Feigelson et al. 2002). The large flare on CXONGC1333 J032859.2+311548 = SVS 16 is discussed in detail in Sect. 6. The lightcurve of XMMU J032810.9+311353 shows a continually decreasing count rate that might reflect rotational modulation. XMMU J032811.0+311730 shows a remarkable double flare, separated by about 4 hours.

4. X-ray spectra and luminosities

For all sources containing at least ~200 source counts we performed a spectral analysis to derive plasma temperatures and X-ray luminosities. With SAS we extracted the pulse hight spectra for each source and a background region, and built the

corresponding redistribution matrix files and ancillary response files. We grouped the spectra with 25 counts per bin and performed joint spectral fits to the background subtracted MOS1, MOS2, and PN spectra of each source with the Sherpa package contained in CIAO. We used the XSPEC model "raymond" describing the emission from a thermal plasma spectrum and "wabs" for the absorption model. We fixed the abundances to a value of 0.3 times solar elemental abundances; this value is typical for young stellar objects (see e.g. Imanishi et al. 2002) and is also supported by our spectral analysis of two bright sources with strong emission lines (CXONGC1333 J032912.9+311815 in Fig. 6 and the flare spectrum of SVS 16 in Fig. 8), for which fits with abundances used as a free parameter also yield a value of ~0.3 times solar.

A single-temperature plasma model plus absorption yielded statistically acceptable fits to most spectra. For the remaining spectra we used two-temperature models, which always gave statistically acceptable fits. We did not consider more complicated spectral models, although we are fully aware that the coronae of active stars are generally not monothermal (e.g. Brickhouse et al. 2000; Sanz-Forcada et al. 2001). The purpose of our analysis was *not* to perform a detailed investigation of the temperature structure of those sources, which is hardly possible given the relatively low numbers of counts per spectrum, but just a simple characterization of the coronal temperature distribution[3]. The fitted plasma temperatures are listed in Table 2, and Fig. 6 shows the spectra of four selected sources, which are representative for our data. The fits generally yield plasma temperatures between ~0.7 keV and ~3 keV for most sources. The spectra of five sources suggest the presence of very hot plasma with $kT > 4$ keV ($T \gtrsim 50 \times 10^6$ K); most of these sources showed flares during the *XMM-Newton* observation. In the spectra of CXONGC1333 J032912.9+311815 (Fig. 6) and of SVS 16 (Fig. 8) we also see a strong emission line at 6.7 keV, which we identify with the K line of Fe XXIV and Fe XXV. The presence of this line directly confirms very high plasma temperatures in excess of 50×10^6 K.

In general, the plasma temperatures we derive for the sources in NGC 1333 are in the typical range for quiescent and flaring young X-ray sources (e.g. Feigelson & Montmerle 1999; Preibisch 1997; Preibisch & Zinnecker 2002) and generally agree (within the errors) with the values determined by G02 from the *Chandra* data.

The spectral fits were also use to compute the intrinsic (extinction-corrected) X-ray luminosities by integrating the model source fluxes over the 0.2−10 keV band. The X-ray luminosities are also listed in Table 2, and range from about 2×10^{29} erg/s up to about 2×10^{31} erg/s, and to even higher values for flaring sources. Again, these numbers are in good agreement with other X-ray observations of young stellar objects (e.g. Feigelson & Montmerle 1999; Preibisch & Zinnecker 2002).

For the objects yielding less than about 200 source counts in the *XMM-Newton* data, for which no X-ray spectral analysis was performed, X-ray luminosities can in principle be estimated from the count rates, but only if reasonable estimates of the the hydrogen column density and the plasma temperature are available. As the extinction of the objects in NGC 1333 varies widely, it is hardly possible to determine reliable X-ray luminosity estimates without further information. Therefore, we will only estimate the X-ray luminosities of the faintest detectable sources. The detection limit depends most strongly on the extinction. For obscured T Tauri stars in NGC 1333, for which we assume typical parameters $N_H = 1 \times 10^{22}$ cm^{-2} ($A_V \sim 5$ mag) and $kT = 2.5$ keV, the detection limit is $L_{X,lim} \sim 4 \times 10^{29}$ erg/s. For much less obscured objects (e.g. weak-line T Tauri stars located at the near side of the cloud), for which we assume typical parameters $N_H = 1 \times 10^{21}$ cm^{-2} ($A_V \sim 0.5$ mag) and $kT = 1$ keV, the detection limit is $L_{X,lim} \sim 5 \times 10^{28}$ erg/s.

5. The different populations of X-ray emitting objects

5.1. Intermediate mass stars

NGC 1333 contains two B-type stars: the B9 star BD +30°549 is the optically brightest member of the region; the B6 star SVS 3 is fainter in the optical due to extinction, but the brightest near-infrared source in NGC 1333. Both B stars were detected by *Chandra*. In our *XMM-Newton* data, BD +30° 549 is only marginally detected as a weak X-ray source; our data are consistent with the *Chandra* results, suggesting an X-ray luminosity of about 10^{29} erg/s (G02). SVS 3, on the other hand, is one of the brightest X-ray sources in our *XMM-Newton* images. A fit the the X-ray spectrum requires two temperature components, one at ~1 keV and a second at ~3 keV, and gives an X-ray luminosity of $L_X \sim 2 \times 10^{31}$ erg/s.

The X-ray detections of these two stars are of special interest, because as intermediate-mass stars they are not expected to show intrinsic X-ray emission: they lack both the magnetically driven X-ray emitting coronae of low-mass stars, and the strong high-mass stellar winds in which internal shocks can cause X-ray emission (see discussion in Preibisch & Zinnecker 2001). The most likely explanation for the observed X-ray emission is that it originates not from the B stars themselves, but from unresolved T Tauri star companions. This interpretation is supported here by the large difference (by a factor of 200) of the X-ray luminosities of the two B-stars.

5.2. T Tauri stars

The majority of the X-ray sources detected in NGC 1333 belongs to the class of T Tauri stars. Their X-ray plasma temperatures (~1–3 keV, higher for flaring sources) and X-ray luminosities (from spectral fits: $\sim 1 \times 10^{29}$ erg/s to $\sim 3 \times 10^{31}$ erg/s) are in the typical range for T Tauri stars in other regions, in particular they are very similar to the properties of the T Tauri stars in IC 348 (Preibisch & Zinnecker 2002).

The brightest X-ray source in the field-of-view is the bright star BD +30°547. According to Cernis (1990), this object is a

---

[3] As demonstrated for example by Peres et al. (2000), fits of simulated spectra based on continuous temperature distributions with simple single-temperature models usually yield temperatures near the peak of the underlying temperature distribution.
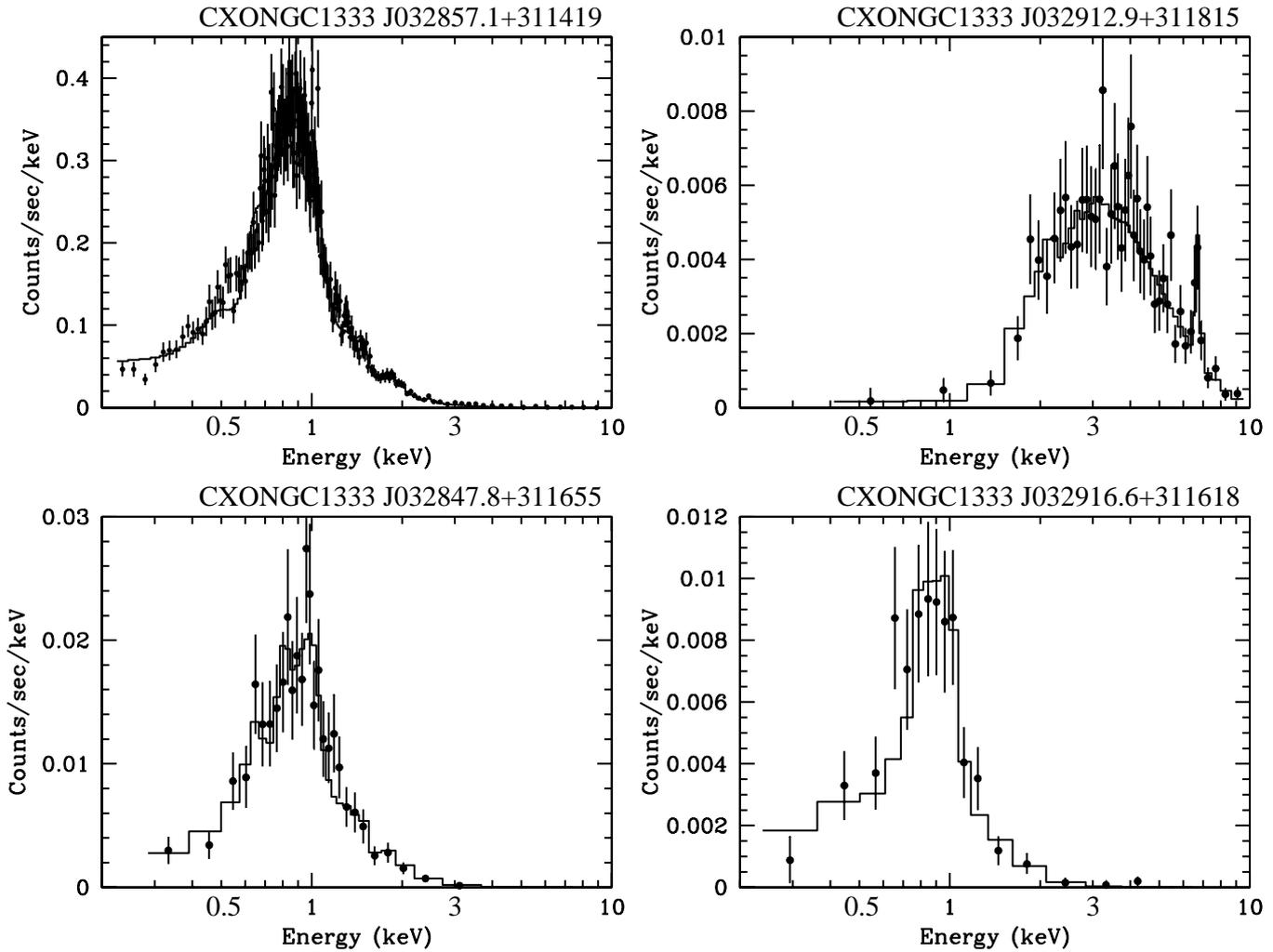
Fig. 6. Some representative *XMM-Newton*-EPIC-PN spectra of X-ray sources in NGC 1333. The solid dots with error bars show the observed spectra, the solid histogram lines show the best fit models. The upper left panel shows the spectrum of the G-type foreground star BD +30°547. The upper right panel shows an optically invisible infrared source which is probably a deeply embedded young stellar object; this source showed a strong flare (see Fig. 5); note the strong emission line at 6.7 keV. The lower plots show the spectra of two moderately obscured optically visible stars.

foreground star at a distance of about 190 pc. The rather low hydrogen column density of $N_H = 2 \times 10^{21}$ cm^{-2} ($A_V \sim 1$ mag) derived from the fit to its X-ray spectrum supports the assumption that BD +30°547 lies in front of the NGC 1333 molecular cloud. The X-ray luminosity (assuming a distance of 190 pc) of 4.9×10^{30} erg/s and the ratio $L_X/L_{bol} = 2 \times 10^{-4}$ are in the typical range for coronally active young stars. The *XMM-Newton* lightcurves of BD +30°547 shows no variability. Interestingly, BD +30°547 is known to be a strongly variable radio source (Rodriguez et al. 1999). In a recent VLA radio observation it showed significant variations on a timescale of hours, which was interpreted as synchrotron emission from an active stellar magnetosphere (Reipurth et al. 2002).

5.3. Protostars

As already reported by G02 and confirmed here in our *XMM-Newton* data, no matches of X-ray sources to one of the known, deeply embedded class 0 or submilimeter protostars in NGC 1333 are found. This is in contrast with the *Chandra* detection of MMS 2 and 3 in the Orion OMC-3 cloud by Tsuboi et al. (2001) and suggest that the protostars in NGC 1333 are weaker X-ray sources or more strongly obscured. The fact that *XMM-Newton* did not detect any embedded object that was not already seen by *Chandra* is also somewhat surprising, given the considerably higher sensitivity of *XMM-Newton* for hard X-rays, which should strongly support the detection of highly obscured objects.

5.4. Unidentified X-ray sources

For 32 X-ray sources no optical or infrared counterpart can be found. These sources are most likely extragalactic objects, for example active galactic nuclei. Their number is consistent with the expected number of extragalactic background X-ray sources (see discussion in G02).

6. The optically invisible source SVS 16

The optically invisible infrared source SVS 16 is one of the most interesting X-ray sources in NGC 1333. Faint X-ray emission from this object was initially detected in the ROSAT HRI observation discussed in Preibisch (1997). As this object was the only optically invisible infrared source in NGC 1333 with a ROSAT detection, we performed a detailed infrared study of SVS 16 (Preibisch et al. 1998), the results of which can be summarized as follows: SVS 16 was resolved into two components separated by 0.99″ at position angle 87.1° (roughly in east-west direction). We obtained near-infrared photometry at UKIRT and found that both components exhibit only a rather small infrared excess. An attempt to detect SVS 16 at $10\,\mu m$ failed and yielded only an upper flux limit. The analysis of K- and H-band spectra of the (unresolved) SVS 16 system obtained at UKIRT yielded a spectral type M2 and suggested an extinction of $A_V = 26$ mag for the brighter western component SVS 16-w. For the fainter eastern component SVS 16-e we estimated a spectral type of ~M3 and an extinction of $A_V \sim 28$ mag. These results suggested that SVS 16 is *not* a system of deeply embedded protostars, but rather of more evolved YSOs that have already cleared at least their inner, hot, circumstellar material. The strong obscuration is either due to cool outer circumstellar material or due to dust in the surrounding cloud environment.

New ROSAT PSPC data confirmed the previous detection with the ROSAT HRI. We estimated the X-ray luminosity by assuming a Raymond-Smith plasma of temperature $kT \sim 1$ keV and a column density of $N_H = 4.7 \times 10^{22}\,\mathrm{cm}^{-2}$ based on the extinction derived from the near-infrared colors. This gave an extremely high X-ray luminosity of about 2×10^{32} erg/s in the 0.1–2.4 keV band. The ROSAT X-ray lightcurves provided no indication of any flaring events or significant variability.

6.1. The X-ray flare on SVS 16

In our *XMM-Newton* images, SVS 16 is the second brightest X-ray source. Inspection of the lightcurve (Fig. 5) shows a huge flare that started near the end of our observation. Figure 7 shows the flare lightcurve in more detail. The PN countrate increased from ~0.05 cnts/s in the pre-flare phase to ~0.7 cnts/s during the flare peak, i.e. by a factor of ~14. In Fig. 7 we also show PN lightcurves extracted in the soft (0.2–2 keV) and hard (2–10 keV) band. It is interesting to note that the peak in the hard band occurs about 25 min before the peak in the soft band. Similar effects have been found flares on the Sun (e.g. Sato 2001; Reale et al. 2001) and on other YSOs (Preibisch & Zinnecker 2002) and can be explained by the the magnetic reconnection flare model: the collision of nonthermal electrons from the coronal reconnection site with chromospheric plasma strongly heats the plasma at the impact site to very high temperatures and causes the emission of hard X-rays. The softer X-ray emission comes from the hot plasma in the postflare loops which are filled only after the impulsive flare phase.

The observed rise phase for the flare on SVS 16 is relatively slow: it extends over 2 hours and can be well described by an
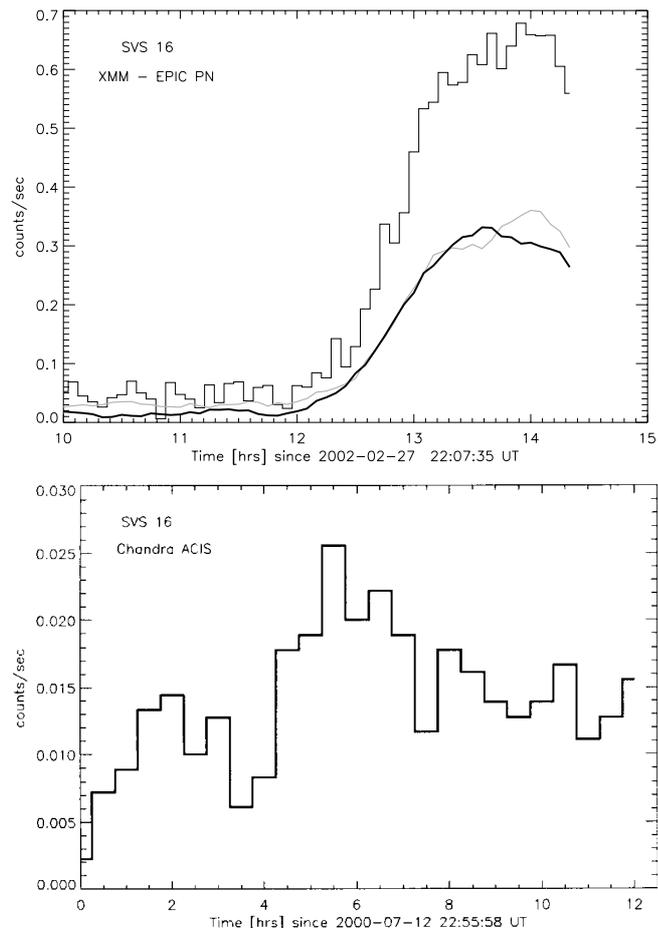
Fig. 7. Upper plot: the *XMM-Newton* lightcurve of SVS16 during the strong flare near the end of our observation. The histogram shows the 0.2–10 keV band background subtracted EPIC PN lightcurve, re-binned into 5 min bins. The grey solid lines shows the smoothed lightcurve in the soft (0.2–2 keV) band, the dark solid lines the smoothed lightcurve in the hard (2–10 keV) band. **Lower plot:** the lightcurve of SVS16 extracted from the archive data of the *Chandra* observation.

exponential rise with a time scale of 0.5 hours. The shape of the rising lightcurve may indicate rotational modulation, i.e. that the flare erupted in a loop that initially was (partly) on the back side of the star and gradually moved into the line of sight due to the stellar rotation (see Stelzer et al. 1999). Unfortunately, the *XMM-Newton* observation terminated shortly after the start of the flare decay phase; therefore it is not possible to model the flare lightcurve to infer some basic parameters of the flaring plasma, such as the plasma density and the length scale of the flaring loop.

We also extracted a lightcurve of SVS 16 from the *Chandra* data (Fig. 7). This lightcurve also shows significant variability and suggests a flare that peaks 5.5 hours after the start of the observation. This flare, however, has a much smaller amplitude than the event seen in the *XMM-Newton* data.
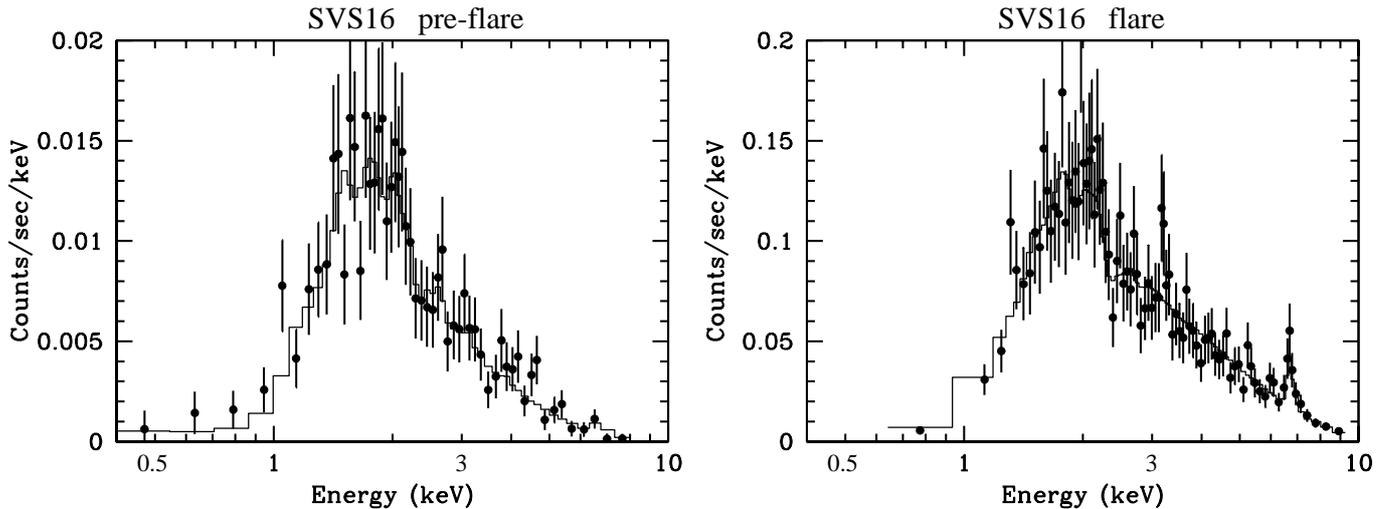
Fig. 8. X-ray spectra of SVS16 in the pre-flare and flare phase. Note the different y-axis scales and the strong 6.7 keV emission line in the flare spectrum.

6.2. The X-ray spectrum of SVS 16

We extracted X-ray spectra for SVS 16 during the flare and during the quiescent phase before the flare (Fig. 8). We first fitted the pre-flare spectrum with a single-temperature plasma model to derive the quiescent temperature T_q. For the fit of the flare spectra we then used a two-component model, in which the temperature and emission measure of the first component was fixed to the values found from the pre-flare spectrum, while the parameters for the second temperature component were allowed to vary. The fit then yields the temperature T_f of the additional X-ray flux that can be attributed to the flare. The fit to the pre-flare spectrum yields $N_H = (1.80\pm0.05)\times10^{22}$ cm^{-2}, $kT_q = (2.32 \pm 0.08)$ keV and results in a quiescent X-ray luminosity of $L_{X,q} = 7.8 \times 10^{30}$ erg/s. For the flare spectrum we find $N_H = (1.95 \pm 0.04) \times 10^{22}$ cm^{-2}, $kT_f = (6.36 \pm 0.35)$ keV. The X-ray luminosity at the flare peak is $L_{X,peak} = 1.4 \times 10^{32}$ erg/s. The very prominent emission line at 6.7 keV in the flare-spectrum probably represents the K line of Fe XXIV and Fe XXV, which is known to trace material at temperatures above 50×10^6 K. The line is already present, although considerably weaker, in the quiescent spectrum; this demonstrates the presence of extremely hot plasma even during the quiescent phase.

We also extracted an X-ray spectrum of SVS 16 from the *Chandra* data. A spectral fit yielded the following parameters: $N_H = (1.63\pm0.08)\times10^{22}$ cm^{-2}, $kT = (2.27\pm0.17)$ keV and results in an X-ray luminosity of $L_X = 5.6\times10^{30}$ erg/s. These parameters are in good agreement with the fitting results reported by G02 and also agree very well to our fit to the *XMM-Newton* pre-flare spectrum.

The most remarkable aspect of these fitting results is the relatively low hydrogen column density, which corresponds to a visual extinction of only $A_{V,(X)} \sim 10$ mag; this is much lower than the extinction determined from the infrared spectrum and photometry of $A_{V,(IR)} = 26-28$ mag. To see how significant this difference is, we computed the covariance matrices of the spectral fits and the corresponding confidence regions in N_H versus

kT space. We found the 3-σ confidence intervals for N_H (correlated) to be $[1.66-1.99] \times 10^{22}$ cm^{-2} for the *XMM-Newton* pre-flare spectrum, and $[1.42-1.95] \times 10^{22}$ cm^{-2} for the *Chandra* spectrum. These results imply that with 99.7% confidence the extinction is below $A_{V,(X)} < 11$ mag, and is therefore, beyond any doubt, inconsistent with the infrared extinction determination of $A_{V,(IR)} = 26-28$ mag (see also G02, who arrived at the same conclusion). Since the infrared extinction value seems equally well constrained as the X-ray spectral fitting result, this inconsistency is quite remarkable. Potential solutions of this problem will be discussed below.

The quiescent X-ray luminosity of SVS 16 derived from the spectral fits to the *Chandra* and *XMM-Newton* data is $L_X \sim 6 \times 10^{30}$ erg/s. This value is considerably lower than the earlier estimate deduced from the ROSAT data and the infrared extinction (see above) and lies within the typical range for X-ray active young stellar objects. The revised X-ray luminosity is also consistent with the non-detection of coronal radio emission from SVS 16 by Smith et al. (1999) and Rodriguez et al. (1999).

6.3. The spatial distribution of the X-ray emission

As SVS 16 is a close binary, one would of course like to know which of the binary components is the X-ray source. With a binary separation of only 1″, this question can definitely not be considered with our *XMM-Newton* data. The *Chandra* data provide a spatial resolution that allows us to obtain at least some, although limited, information on that question. We started our analysis of the *Chandra* archive data by creating a new (level-2) events file in which we removed the ±0.5 pixel randomization, which is applied in standard data processing. We then compared the position of SVS 16 determined from HST/WFPC archive images (datasets U2LS0105T and U2LS0106T) with the *Chandra* image. Two other, apparently single stars in the HST image with X-ray counterparts could be used to align the *Chandra* and HST coordinate systems with an estimated

astrometric accuracy of $\sim 0.1''$. The centroid of the SVS 16 X-ray source position (SVS 16-X hereafter) is located just between the optical components of SVS 16, with an offset of $0.74''$ to the west of SVS 16-e and $0.30''$ to the east of SVS 16-w. This is a first indication that both stars contribute to the X-ray emission.

We also measured the *FWHM* of SVS 16-X and found values of $2.12''$ and $1.84''$ in x and y (RA and Dec) direction, respectively[4]. Comparison to several other sources at similar off-axis angles in the *Chandra* image suggests that SVS 16-X is slightly more extended, another indication of a double source. To investigate this in more detail, we used the MARX *Chandra* data simulator[5] to simulate images of artificial single and double X-ray sources at the location of SVS 16. These simulations took into account the parameters of the actual observation, in particular, we used the original aspect solution data. The simulations showed that the PSF of a single point source at the location of SVS 16 should actually be slightly narrower (*FWHM* of $1.82''$ and $1.78''$ in x- and y-direction) than observed for SVS 16-X. Two equally strong X-ray sources at the locations of SVS 16-w and SVS 16-e, on the other hand, should produce a slightly wider PSF (*FWHM* of $2.51''$ and $1.89''$) than observed. Further simulations showed that the observed PSF of SVS 16-X is most consistent with the assumption of a double X-ray source in which the secondary component is several times (but not orders of magnitude) fainter than the brighter component.

If this interpretation is correct, the X-ray spectrum of SVS 16 is the sum of two different sources. Might this provide a solution to the "extinction problem"? If the intrinsic spectra of the two components would be very different, e.g. if one source would have a much softer spectrum and suffer much less extinction than the other source, the fit to the combined spectrum might, in principle, underestimate the extinction significantly. However, since the infrared properties of SVS 16-w and SVS 16-e are quite similar and there is no indication of significantly different extinctions, we have no reason to assume that both components are intrinsically very different.

6.4. Clues to the X-ray emission process

How can we understand the X-ray properties of SVS 16, especially the strong discrepancy of the infrared and X-ray extinction estimates? We first consider possible geometries of the circumstellar material around SVS 16 and then different possibilities for the origin of the X-ray emission. As described above, the lack of strong near- or mid-infrared excesses and strong veiling in the near-infrared spectra shows that the amount of hot or warm circumstellar matter close to the stars must be small. Nevertheless, the observational data do not exclude the possible presence of relatively cool ($T \lesssim 300$ K)

circumstellar matter at distances of more than ~ 10 AU from the stars. For example, a disk with an inner hole of radius $R_{\rm in} \sim 20$ AU around one or both stars would cause significant infrared excess emission only at wavelengths above $10\,\mu$m. If such a disk[6] would be seen nearly edge on, it could explain the strong obscuration of the stellar fluxes.

An alternative possibility is that there is no circumstellar material in the system and the obscuration is due to dust in the local cloud environment. A rough estimate of the column density of the cloud along the line-of-sight to SVS 16 can be made from the 1.25 mm map of NGC 1333 presented by Lefloch et al. (1998). Comparison of the 1.25 mm flux at the position of SVS 16 with the flux in the nearby core called Cor1 suggests that the cloud column density in the direction of SVS 16 is about $N_{\rm H,(cloud)} = 1.4 \times 10^{22}$ cm^{-2}. This value is an upper limit to the column density along the line-of-sight towards SVS 16 and is roughly consistent with the column density derived from the X-ray spectra, but much lower than the extinction implied from the infrared colors. This suggests that some part of the strong obscuration of the stellar fluxes is actually caused by circumstellar matter rather than by intra-cloud material.

Now let us consider different possibilities for the origin of the X-ray emission.

6.4.1. Colliding stellar winds or outflows

One possibility is that the X-ray emission originates from colliding winds or outflows in the region between the two binary components. Strong X-ray emission from colliding stellar winds is frequently observed in very tight O-star binary systems (e.g. Zhekov & Skinner 2000). Although the low-mass stars in SVS 16 must have much weaker and slower winds, and although their separation (~ 310 AU) is quite large, the model calculations of Zhekov et al. (1994) suggest that colliding winds in a system like SVS 16 might, under favorable conditions, produce soft X-ray emission at levels of some 10^{29} erg/s.

This scenario would, in principle, offer an elegant solution of the "extinction problem", because the light from the stars could be strongly obscured by circumstellar material, whereas the X-rays emitted in the wind collision zone between the two stars would only suffer from the much lower extinction in the intra-cloud material. However, the model can neither explain the high X-ray luminosity of SVS 16 and the hot plasma temperatures[7], nor can it account for the observed X-ray flaring; these properties clearly require that at least the bulk of the X-ray emission is caused by some kind of magnetic activity.

Perhaps, the observed X-ray emission from SVS 16 is a combination of coronal emission from the young stars and some soft X-ray emission from colliding wind/outflow shocks;

---

[4] These values are clearly larger than the nominal mirror PSF because the image is blurred by small residual errors in the reconstruction of the *Chandra* aspect solution.

[5] Further information on the MARX simulator can be found at `http://space.mit.edu/CXC/MARX/`.

[6] We note that there is also a constraint on the outer radius of a hypothetical disk, because the maximum size of the circumstellar disks in a binary system is expected to be at most about 1/3 of the binary separation, i.e. ~ 100 AU in the case of SVS 16. However, since we do not know the projection angle under which we look at the system, this value might be substantially larger.

[7] The observed plasma temperature of $\sim 25 \times 10^6$ K would require wind velocities of the order of $\gtrsim 1000$ km s^{-1}, much larger than typical for low-mass stars.

this shock emission would then produce a soft excess in the X-ray spectrum that could help to explain the low X-ray extinction estimate.

6.4.2. X-ray scattering in the circumbinary environment

Another possibility is that the X-ray emission from the stars is not seen directly, but scattered into the line-of-sight by outer, circumbinary material. One might imagine favorable geometries in which the scattered X-rays would then suffer much less extinction than the direct light from the stars that is strongly obscured by circumstellar disks seen nearly edge on. This scenario was considered by Bally et al. (2003) to explain the difference between X-ray and infrared extinction in the protostellar binary system L1551 IRS 5.

While this scenario can certainly not be excluded, we note that there is, at least so far, no direct evidence for any circumstellar or circumbinary material in the SVS 16 system. Also, as the scattering takes place relatively far from the stars, one would expect the X-ray emission to be offset from the positions of the stars; such an positional offset is observed in L1551 IRS 5, but not in SVS 16.

6.4.3. X-ray emitting plasma displaced from the stellar surface

Might it be possible that a peculiar circumstellar structure absorbs much of the optical/infrared flux from the stellar disk, but not the X-ray flux that might originate from an extended structure above the stellar surface, e.g. from a giant coronal loop? To explore this possibility, we need to estimate the size of the X-ray emitting region. The volume V of the X-ray emitting plasma can be estimated from the emission measure EM that was found in the fit to the X-ray spectrum, and the mean plasma density n, which are related by $EM \sim n^2 V$. Since our X-ray data do not provide us with direct information about the plasma densities, we will consider the typical range of plasma densities in the coronae of late type stars, $n \sim [10^9 \ldots 10^{12}]$ cm^{-3} (see e.g. discussion in Drake et al. 2000). We then can estimate a characteristic size r for the X-ray emitting region by assuming for example a simple spherical distribution, i.e. $V = \frac{4\pi}{3} r^3$.

The emission measure derived from the *Chandra* fit to the quiescent X-ray spectrum of SVS 16 is 4.71×10^{53} cm^{-3}. The resulting volumes are therefore $V \approx [4.7 \times 10^{29} \ldots 4.7 \times 10^{35}]$ cm^3 and the corresponding sizes are $r \approx [4.8 \times 10^9 \ldots 4.8 \times 10^{11}]$ cm, what corresponds to $\sim [0.014 \ldots 1.4] \times$ the stellar radius of $R_* \sim 5.2 R_\odot$ for SVS 16-w (Preibisch et al. 1998). If the X-ray emitting star were surrounded by a homogeneous shell of coronal plasma, this shell would have an outer radius of at most $1.5 R_*$.

In more realistic magnetic loop geometries, emission measure and characteristic length scale l are related through $EM = N\alpha^2 n^2 l^3$, where N denotes the number of coronal loops and α the loop aspect ratio. Assuming that all X-ray emission comes from a single giant loop, i.e. $N = 1$, and using $\alpha = 0.1$,

the derived length scale would be $l = [3.6 \times 10^{10} \ldots 3.6 \times 10^{12}]$ cm = $[0.1 \ldots 10] R_*$.

We conclude from this analysis that the size of the X-ray emitting plasma must by rather compact and can hardly be displaced by more than a few stellar radii from the stellar surface. If a circumstellar disk were to occult the star but not a coronal loop extending a few stellar radii above the stellar surface, this disk would have to be extremely flat and be seen exactly edge on. While we cannot exclude such a scenario, it appears very unlikely.

6.4.4. Conclusions on the origin of the X-rays

None of the scenarios explored above provides a satisfying explanation for the observed X-ray properties of SVS 16. Perhaps, a combination of different effects is at work, e.g. some X-ray scattering plus a contribution from colliding winds. Possible alternative explanations might also include a non-canonical dust-to-gas ratio[8], or perhaps some rapid process that has changed the circumstellar environment of SVS 16 between the time of our infrared study in 1997 and the *Chandra* and *XMM-Newton* observations 3 to 5 years later.

7. No X-ray emission from HH7-11

An interesting characteristic of the NGC 1333 star forming region is the presence of the numerous outflows and Herbig-Haro (HH) objects (see e.g. Bally et al. 1996; Bally & Reipurth 2001; Hodapp & Ladd 1995). Pravdo et al. (2001) recently reported the first X-ray discovery of a Herbig-Haro object, HH 2, with *Chandra*. The derived X-ray luminosity is a few times 10^{29} erg/s, and the X-ray spectrum is rather soft, consistent with the idea that the emission originates from shock-heated material at the leading edge of the jet bow shock with temperatures of $\sim 10^6$ K. Favata et al. (2002) claimed the detection of X-ray emission from the HH 154 jet in a *XMM-Newton* observation of the L1551 region. However, a *Chandra* observation (Bally et al. 2003) recently showed that the X-rays do not come from the jet knot but from a compact source located at the base of the jet. The X-ray detection of further HH objects would strongly improve the understanding of the processes giving rise to the observed emission.

None of the *Chandra* and *XMM-Newton* X-ray sources in NGC 1333 can be identified with HH objects (see also G02). In order to see whether we can find faint extended X-ray emission, that might have been missed by the source detection routines, we carefully investigated the region of the HH 7-11 chain of HH objects, the most prominent jet in the NGC 1333 region. We defined four circular areas with $3''$ to $5''$ radii centered on

---

[8] We note that Bary et al. (2002) recently reported the detection of molecular hydrogen gas orbiting the weak-line T Tauri star DoAr 21; this object shows no thermal emission from circumstellar dust and was heretofore presumed to be nearly devoid of circumstellar material. This discovery provides evidence for a deviation from the usual dust-to-gas ratio, which is the basis of the canonical relation between hydrogen column density and extinction. However, in order to explain the properties of SVS 16, we need exactly the opposite situation, i.e. an essentially gas-free dust disk.

the optically brightest parts of HH 7, HH 8, HH 10 and HH 11 and compared the numbers of counts in these area to the local background. None of these regions shows a significant excess of counts over the expected background values. From the *Chandra* data we derive upper limits of <0.33 cnts/ksec for HH 7[9], <0.05 cnts/ksec for HH 8, <0.10 cnts/ksec for HH 10, and <0.07 cnts/ksec for HH 11. In the *XMM-Newton* data we find upper limits to the MOS1+MOS2+PN countrates of <0.13 cnts/ksec for HH 7, <0.09 cnts/ksec for HH 8, <0.05 cnts/ksec for HH 10, and <0.05 cnts/ksec for HH 11.

Is the non-detection of X-ray emission from HH 7-11 surprising? X-ray emission at levels similar to that of HH 2 or HH 154 should clearly be detectable in our data. The most important physical differences between HH 7-11 on the one hand and HH 2/HH 154 on the other hand are the rather low shock velocities ($\lesssim 40$–50 km s^{-1}; see Noriega-Crespo & Garnavich 2001) and the correspondingly low-excitation nature (e.g. Molinari et al. 2000; Solf & Böhm 1987) of the HH 7-11 chain, in contrast to the considerably higher shock velocities (~ 150–200 km s^{-1}) and higher excitation in HH 2 and HH 154. In a recent paper, Raga et al. (2002) describe a simple analytic model for predicting the X-ray luminosity of a bow shock from the parameters of the flow, that fits the observed X-ray fluxes from HH 2 and HH 154 well. For the parameters of HH 7-11 (taken from Solf & Böhm 1987; Molinari et al. 2000 and Noriega-Crespo & Garnavich 2001), i.e. shock velocities $v_{\mathrm{bs}} \sim 50$ km s^{-1}, densities $n_{\mathrm{e}} \sim 220$–1300 cm^{-3}, and radii $r_{\mathrm{b}} \sim 0.5 - 1 \times 10^{16}$ cm, the model by Raga et al. (2002) predicts X-ray luminosities of less than $\approx 1 \times 10^{27}$ erg/s; this is clearly below the sensitivity limit of the *Chandra* and *XMM-Newton* observations. Another aspect is that the expected shock temperatures (Eq. (2) in Raga et al. 2002) for HH 7-11 are only 24 000 K to 54 000 K, i.e. more than one order of magnitude lower than the expected shock temperature for HH 2 and HH 154. Therefore, any high-energy emission from HH 7-11 should be extremely soft, with most of the flux below the passbands of *Chandra* and *XMM-Newton*.

8. Summary and conclusions

Our deep *XMM-Newton* observation of NGC 1333 confirms the *Chandra* results recently obtained by G02. Despite the higher sensitivity of *XMM-Newton* for hard X-ray emission as expected from deeply embedded young stellar objects, none of the known protostars in NGC 1333 is detected. For the optically invisible infrared source SVS 16, the remarkable inconsistency of the hydrogen column density derived from the X-ray spectrum and the extinction determined from the infrared photometry and spectroscopy remains puzzling. In agreement with the *Chandra* results, we find that the (quiescent) X-ray luminosity is much smaller than suspected earlier. SVS 16 showed a

spectacular X-ray flare during our observation; the unfortunate fact that the observation terminated shortly after the flare peak, however, prevented a detailed analysis. The non-detection of X-ray emission from HH 7-11 can probably be understood as a consequence of the low-velocity and low-excitation nature of these shocks.

References

Aspin, C., Sandell, G., & Russel, A. P. G. 1994, A&AS, 106, 165
Bally, J., & Reipurth, B. 2001, ApJ, 546, 299
Bally, J., Devine, D., & Reipurth, B. 1996, ApJ, 473, L49
Bally, J., Feigelson, E., & Reipurth, B. 2003, ApJ, in press
Bary, J. S., Weintraub, D. A., & Kastner, J. H. 2002, ApJ, 576, L73
Brickhouse, N. S., Dupree, A. K., Edgar, R. J., et al. 2000, ApJ, 530, 387
Cernis, K. 1990, Ap&SS, 166, 315
Chini, R., Ward-Thompson, D., Kirk, J. M., et al. 2001, A&A, 369, 155
Drake, J. J., Peres, G., Orlando, S., Laming, M., & Maggio, A. 2000, ApJ, 545, 1074
Favata, F., Fridlund, C. V. M., Micela, G., Sciortino, S., & Kaas, A. A. 2002, A&A, 386, 204
Feigelson, E. D., & Montmerle, T. 1999, ARA&A, 37, 363
Feigelson, E. D., Garmire, G. P., & Pravdo, S. H. 2002, ApJ, 572, 335
Freeman, P. E., Kashyap, V., Rosner, R., & Lamb, D. Q. 2002, ApJS, 138, 185
Getman, K. V., Feigelson, E. D., Townsley, L., et al. 2002, ApJ, 575, 354 [G02]
Herbig, G. H. 1998, ApJ, 497, 736
Herbig, G. H., & Jones, B. F. 1983, AJ, 88, 1040
Hodapp, K.-W. 1994, ApJS, 94, 615
Hodapp, K.-W., & Ladd, E. F. 1995, ApJ, 453, 715
Imanishi, K., Tsujimoto, M., & Koyama, K. 2002, ApJ, 572, 300
Jansen, F., Lumb, D., Altieri, B., et al. 2001, A&A, 365, L1
Jones, B. F., & Herbig, G. H. 1982, AJ, 87, 1223
Knee, L. B. G., & Sandell, G. 2000, A&A, 361, 671
Kraft, R. P., Burrows, D. N., & Nousek, J. A. 1991, ApJ, 374, 344
Lada, C. J., Gottlieb, C., Litvak, M., & Lilley, A. E. 1974, ApJ, 194, 609
Lada, E. A., Alves, J., & Lada, C. J. 1996, AJ, 111, 1964
Lefloch, B., Castets, A., Cernicharo, J., Langer, W. D., & Zylka, R. 1998, A&A, 334, 269
Looney, L. W., Mundy, L. G., & Welch, W. J. 2000, ApJ, 529, 477
Molinari, S., Noriega-Crespo, A., Ceccarelli, C., et al. 2000, ApJ, 538, 698
Montmerle, T., Koch-Miramond, L., Falgarone, E., & Grindlay, J. E. 1983, ApJ, 269, 182
Noriega-Crespo, A., & Granavich, P. 2001, AJ, 122, 3317
Peres, G., Orlando, S., Reale, F., Rosner, R., & Hudson, H. 2000, ApJ, 528, 537
Pravdo, S. H., Feigelson, E. D., Garmire, G., et al. 2001, Nature, 413, 708
Preibisch, Th. 1997, A&A, 324, 690
Preibisch, Th., & Zinnecker, H. 2001, AJ, 122, 866
Preibisch, Th., & Zinnecker, H. 2002, AJ, 123, 1613

---

[9] A 5″ radius circle at the position of HH 7 contains 12 photons in the 0.1–10 keV band, whereas the expected background value is only 4.5 photons. However, we do not believe that this indicates X-ray emission from HH 7, because 8 of the 12 photons have energies above 2 keV, whereas the soft X-ray emission from an HH object should give almost exclusively soft (<1 keV) photons. The accumulation of photons seems to be a random background fluctuation.

Preibisch, Th., Zinnecker, H., & Herbig, G. H. 1996, A&A, 310, 456

Preibisch, Th., Neuhäuser, R., & Stanke, Th. 1998, A&A, 338, 923

Preibisch, Th., & Neuhäuser, R. 1995, in Flares and Flashes, ed. J. Greiner, H. Duerbeck, & R. E. Gershberg (Berlin: Springer), IAU Coll., 151, 212

Raga, A. C., Noriega-Crespo, A., & Velazquez, P. F. 2002, ApJ, 576, L149

Raymond, J. C., & Smith, B. W. 1977, ApJS, 35, 419

Reale, F., Peres, G., & Orlando, S. 2001, ApJ, 557, 906

Reipurth, B., Rodriguez, L. F., Anglada, G., & Bally, J. 2002, AJ, 124, 1045

Rodriguez, L. F., Anglada, G., & Curiel, S. 1999, ApJS, 125, 427

Sanz-Forcada, J., Brickhouse, N. S., & Dupree, A. K. 2001, ApJ, 554, 1079

Sato, J. 2001, ApJ, 558, L137

Smith, K., Güdel, M., & Benz, A. O. 1999, A&A, 349, 475

Solf, J., & Böhm, K. H. 1987, AJ, 93, 1172

Stelzer, B., Neuhäuser, R., Casanova, S., & Montmerle, T. 1999, A&A, 344, 154

Strom, S. E., Vrba, F., & Strom, K. M. 1976, AJ, 81, 314

Strüder, L., Briel, U., Dennerl, K., et al. 2001, A&A, 365, L18

Tsuboi, Y., Koyama, K., Hamaguchi, K., et al. 2001, ApJ, 554, 734

Turner, M. J. L., Abbey, A., Arnaud, M., et al. 2001, A&A, 365, L27

Warin, S., Castets, A., Langer, W. D., Wilson, R. W., & Pagani, L. 1996, A&A, 306, 935

de Zeeuw, P. T., Hoogerwerf, R., de Bruijne, J. H. J., Brown, A. G. A., & Blaauw, A. 1999, AJ, 117, 354

Zhekov, S. A., & Skinner, S. L. 2000, ApJ, 538, 808

Zhekov, S. A., Palla, F., & Myasnikov, A. V. 1994, MNRAS, 271, 667